

This work was written as part of one of the author's official duties as an Employee of the United States Government and is therefore a work of the United States Government. In accordance with 17 U.S.C. 105, no copyright protection is available for such works under U.S. Law.

CC0 1.0 Universal (CC0 1.0)
Public Domain Dedication

<https://creativecommons.org/publicdomain/zero/1.0/>

Access to this work was provided by the University of Maryland, Baltimore County (UMBC) ScholarWorks@UMBC digital repository on the Maryland Shared Open Access (MD-SOAR) platform.

Please provide feedback

Please support the ScholarWorks@UMBC repository by emailing scholarworks-group@umbc.edu and telling us what having access to this work means to you and why it's important to you. Thank you.

SOFIA mid-infrared observations of Supernova 1987A in 2016 – forward shocks and possible dust re-formation in the post-shocked region

Mikako Matsuura¹,¹★ James M. De Buizer,² Richard G. Arendt,^{3,4} Eli Dwek,³ M. J. Barlow⁵,⁵ Antonia Bevan⁵, Phil Cigan,¹ Haley L. Gomez,¹ Jeonghee Rho,^{2,6} Roger Wesson,⁵ Patrice Bouchet,^{7,8} John Danziger⁹ and Margaret Meixner^{10,11}

¹School of Physics and Astronomy, Cardiff University, Queen's Buildings, The Parade, Cardiff, CF24 3AA, UK

²Stratospheric Observatory For Infrared Astronomy NASA Ames Research Center, MS 232-12 Moffett Field, CA 94035, USA

³Observational Cosmology Lab, Code 665, NASA Goddard Space Flight Center, Greenbelt, MD 20771, USA

⁴University of Maryland, Baltimore County, Baltimore, MD 21250, USA

⁵Department of Physics and Astronomy, University College London, Gower Street, London WC1E 6BT, UK

⁶SETI Institute, 189 N. Bernardo Avenue, Mountain View, CA 94043, USA

⁷DRF/IRFU/Dap, CEA-Saclay, F-91191 Gif-sur-Yvette, France

⁸NRS/AIM, Université Paris Diderot, F-9119 Gif-sur-Yvette, France

⁹Osservatorio Astronomico di Trieste, Via Tiepolo 11, Trieste 34143, Italy

¹⁰Space Telescope Science Institute, 3700 San Martin Drive, Baltimore, MD 21218, USA

¹¹Department of Physics and Astronomy, The Johns Hopkins University, 366 Bloomberg Center, 3400 N. Charles Street, Baltimore, MD 21218, USA

Accepted 2018 October 1. Received 2018 September 25; in original form 2017 November 30

ABSTRACT

The equatorial ring of Supernova (SN) 1987A has been exposed to forward shocks from the SN blast wave, and it has been suggested that these forward shocks have been causing ongoing destruction of dust in the ring. We obtained Stratospheric Observatory For Infrared Astronomy The Faint Object InfraRed Camera for the SOFIA Telescope (FORCAST) 11.1, 19.7, and 31.5 μm photometry of SN 1987A in 2016. Compared with *Spitzer* measurements 10 yr earlier, the 31.5 μm flux has significantly increased. The excess at 31.5 μm appears to be related to the *Herschel* 70 μm excess, which was detected 5 yr earlier. The dust mass needed to account for the 31.5–70 μm excess is $3\text{--}7 \times 10^{-4} M_{\odot}$, more than 10 times larger than the ring dust mass ($\sim 1 \times 10^{-5} M_{\odot}$) estimate from the data 10 yr earlier. We argue that dust grains are re-formed or grown in the post-shock regions in the ring after forward shocks have destroyed pre-existing dust grains in the ring and released refractory elements into gas. In the post-shock region, atoms can stick to surviving dust grains, and the dust mass may have increased (grain growth), or dust grains might have condensed directly from the gas. An alternative possibility is that the outer part of the expanding ejecta dust might have been heated by X-ray emission from the circumstellar ring. The future development of this excess could reveal whether grains are reformed in the post-shocked region of the ring or eject dust is heated by X-ray.

Key words: circumstellar matter – supernovae: individual: Supernova 1987A – dust – ISM: supernova remnants – infrared: stars.

1 INTRODUCTION

It has been proposed that core-collapse supernovae (SNe) play a dual role in the production and destruction of the dust in the interstellar media (ISM) of galaxies, and currently, these contradictory roles are subjects of intense investigations. It has been proposed that a large mass ($0.1\text{--}1 M_{\odot}$) of dust can be formed in SN ejecta, using

newly synthesized elements, thus, SNe can be an important source of dust in the ISM of galaxies (Morgan & Edmunds 2003; Nozawa et al. 2003; Dwek & Cherchneff 2011). In parallel, theories have predicted that SN blast waves should destroy ISM dust grains by sputtering (e.g. Barlow 1978; Schneider, Ferrara & Salvaterra 2004; Bocchio, Jones & Slavin 2014), with only larger grains surviving. Jones et al. (1994) found that SN shocks could destroy ~ 95 per cent of ISM dust grains, resulting in a lifetime of dust grains in the ISM to be a few hundred million years. Temim et al. (2015) suggested much shorter dust lifetimes in the Magellanic Clouds (a few

* E-mail: matsuura@cardiff.ac.uk

10 Myr). On the other hand, recent full hydrodynamical modelling (Silvia, Smith & Shull 2012; Slavin, Dwek & Jones 2015) has found much longer ISM grain lifetimes (>1 Gyr) against destruction by SN shocks. Although the lifetime of ISM dust is one of the keys in understanding dust evolution in galaxies, dust lifetimes are still uncertain (Micelotta et al. 2017), owing to limited understanding of SN dust destruction processes.

Divided ideas about dust formation and destruction in SNe and SN remnants (SNRs) are also found in observations. SN 1987A was the first SN in which dust formation was reported (Danziger et al. 1989). Since then dust formation has been reported in over 10 SNe and a few SNRs (Gall et al. 2014; Matsuura 2017; Sarangi, Matsuura & Micelotta 2018) with the inferred dust masses in young SNe typically of the order of 10^{-6} to $10^{-3} M_{\odot}$ (e.g. Wooden et al. 1993; Bouchet et al. 2004; Kotak et al. 2009). Twenty three years after the explosion, a large mass ($\sim 0.5 M_{\odot}$) of cold (~ 22 K) ejecta dust was found by far-infrared observations in SN 1987A (Matsuura et al. 2011). After this finding of a large dust mass, the evolution of the dust mass of SN 1987A was re-visited, and now there is a debate as to whether such a large mass of dust was present in early days but the dust emission was optically thick and the inferred dust mass was underestimated (Dwek & Arendt 2015; Sluder, Milosavljević & Montgomery 2016). An alternative possibility is that the dust mass was indeed small at early times and increased over time (Wesson et al. 2014; Bevan & Barlow 2016).

Dust destruction by SNRs has been predicted by theories, but its measurement is challenging. Lakicevic et al. (2015) analysed dust in the SNRs in the Large Magellanic Cloud, and found that the ISM dust mass towards the SNRs tended to be lower than for the surrounding regions. They claimed that SNRs may destroy more dust than they produce. However, their finding of a reduced dust mass towards the SNRs may be attributable to hot SNR emission overwhelming cold ISM dust emission, thus it may not be conclusive that the analysis shows dust destruction by SNRs (Matsuura et al. 2016; Micelotta et al. 2017). Modelling *Spitzer's* (Werner et al. 2004) emission of old Galactic SNRs (the Cygnus Loop and the Puppis A), Sankrit et al. (2010), and Arendt et al. (2010) estimated that about 35 per cent and 25 per cent of dust grains have been destroyed. Meanwhile, Lau et al. (2015) suggested that dust had survived the reverse shock in the $\sim 10\,000$ yr old Galactic SNR, Sgr A East. Following the detection of CO molecules in the reverse shock region of the Galactic SNR, Cassiopeia A (Rho et al. 2009; Wallström et al. 2013), chemical models have predicted that CO molecules can re-form in the post-shock regions but that it would be difficult to re-form dust in this SNR (Biscaro & Cherchneff 2014).

The explosion of SN 1987A was detected in the Large Magellanic Cloud, that lies only 50 kpc away. Due to its close distance, SN 1987A provides a unique opportunity to monitor at almost all wavelengths how the SNR has evolved over the past 30 yr. *Hubble Space Telescope* (HST) optical images showed that the SNR is composed of ejecta, an equatorial circumstellar ring and two fainter outer rings. The ring is thought to consist of the material lost from the progenitor via a stellar wind when the star was in the red-supergiant phase 20 000–40 000 yr ago (Arnett et al. 1989; McCray 1993). While the ejecta are expanding at about 2000 km s^{-1} on average, the equatorial ring (hereafter the ring) expands much more slowly (about $10\text{--}100 \text{ km s}^{-1}$). The HST monitoring programme captured the ejecta expansion as its appearance changed from a single blob in the 1990s to a keyhole shape in the 2000s. Finally, the fastest part of the forward shock has passed the ring, with shock heated material just outside the ring in a 2014 image (Fransson et al. 2015).

For SN 1987A, dust is found not only in the ejecta but also in the equatorial ring. Bouchet et al. (2006) obtained spatially resolved images at 11.7 and 18.3 μm , and identified silicate warm dust (~ 180 K) emission (Fig. 1) mainly arising from the ring. Additionally, *Spitzer Space Telescope* observations found continuous emission between 3.6 and 4.5 μm , and this component is attributed to collisionally heated dust in the ring (Dwek et al. 2010), with a temperature of ~ 525 K (Arendt et al. 2016). In contrast, Atacama Large Millimeter Array (ALMA) resolved images revealed that cold (~ 22 K; Matsuura et al. 2015) dust emission clearly originates from the ejecta (Indebetouw et al. 2014; Zanardo et al. 2014). SN 1987A has at least three discrete dust components in terms of temperature (Fig. 1), and two in terms of location: the ring and the ejecta.

Over the last 12 yr, *Spitzer* has monitored emission from the ring dust at 6-month intervals (Dwek et al. 2010; Arendt et al. 2016). After its launch in 2003, *Spitzer* detected increasing fluxes from 3.6 to 24 μm . After the liquid helium ran out in 2009, *Spitzer* continued to monitor only at 3.6 and 4.5 μm , and has found an increasing trend of hot dust components until day ~ 9000 , when the fluxes started decreasing (Arendt et al. 2016). *Spitzer* observations have provided unique insights into the interaction between the SN blast wave and pre-existing material in the ring.

The infrared emission of the ring arises from ~ 180 K silicate dust grains, collisionally heated by the SN blast wave (Bouchet et al. 2006). The same collisions are also capable of destroying the dust by thermal sputtering (Dwek et al. 2008). Recently, Arendt et al. (2016) reported that while the hot component has reduced its 3.6 and 4.5 μm fluxes since ~ 2012 , the X-ray radiation, which is the heating source of dust, remains constant. They proposed that some dust grains in the ring have been destroyed. Theory (Dwek et al. 2010) predicts that these dust grains are expected to be destroyed by sputtering within ~ 1 yr. The existence of a hot component over a period of more than 3 yr suggests that ambient circumstellar material is continuously being swept up by the shocks, acquiring more circumstellar dust. The monitoring of the ring dust emission has detected changes over a more than 10 yr time-scale.

Here, we report Stratospheric Observatory For Infrared Astronomy (SOFIA) photometry observations of SN 1987A's dust at 11.1, 19.7, and 31.5 μm obtained in 2016 June, after resumption of mid-IR monitoring.

2 OBSERVATIONS

SN 1987A was observed with the NASA SOFIA (Young et al. 2012) in the 2016 Cycle 4 observing cycle during a deployment to the Southern hemisphere where the aircraft was temporarily based in Christchurch, New Zealand. Observations of SN 1987A were taken on two separate flights (Flight 318 and 320). These flight numbers correspond to taking off in 2016 July 11 (day 10 731 since the explosion of SN 1987A) and 2016 July 13 (day 10 733). The observations were performed with the FORCAST imager and spectrometer (Herter et al. 2012) using the FOR_F111, FOR_F197, and FOR_F315 filters. FORCAST has a short wavelength camera that is optimized to observe at wavelengths from 5 to 25 μm , and a long wavelength camera optimized for observations from 25 to 40 μm . All imaging observations were performed using the dual channel mode of FORCAST, which employs a dichroic to allow imaging in both cameras simultaneously. The 31.5 μm filter remained in the long wavelength camera for all observations, while the short wavelength camera was configured to observe either in the 11.1 or 19.7 μm filter. Both cameras have 256×256 pixels, which after distortion correction yield an effective field of view of $3.4' \times 3.2'$.

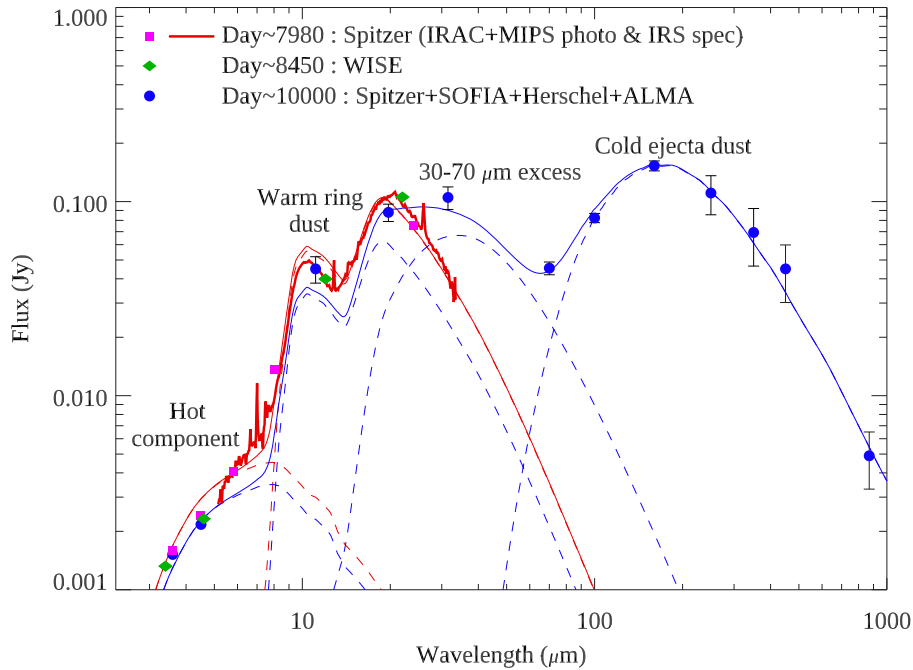


Figure 1. The near- to far-infrared SED of SN 1987A at three different epochs, with fitted dust models. The pink squares and thick red line show the *Spitzer* Infrared Array Camera (IRAC) and Multiband Imaging Photometer (MIPS) photometry data and IRS spectrum at day ~ 7980 (Dwek et al. 2010), with the model fits as thin red lines (model 1 in Table 2). *WISE* data at day 8450 are plotted as green diamonds. The blue circles show flux measurements around day 10 000, assembled from *Spitzer* IRAC 3.6 and 4.5 μm data at day 10 377 (Arendt et al. 2016), *Herschel* measurements at day 9090 (Matsuura et al. 2015), ALMA measurements at 850 and 450 μm at day 9294 and 9351 (Zanardo et al. 2014), and our SOFIA observations at day 10 732. One- σ uncertainties are plotted. The blue lines show four dust-component fits to the SED at day $\sim 10\,000$, with individual components plotted as dashed blue lines (model 2 in Table 2).

with a pixel scale of $0.768' \text{ pixel}^{-1}$. Observations were performed using the ‘Nod-Match-Chop’ mode (a standard thermal infrared chop-nod background subtraction technique), and were configured to have 45' East–West chop and nod throws.

Though co-added and calibrated pipelined data products were produced by the SOFIA Data Cycle System, the preliminary investigation of the data did not show detections at the signal-to-noise level expected. In particular, while there was a clear detection of SN 1987A at 31 μm from the first flight, there was no clear detection of it at that wavelength on the second flight, even though the observing time in this filter was comparable on both flights. The instrumental sensitivities in these filters are predominantly correlated to the water vapour overburden, with the 31.5 μm filter being the most negatively affected by high water vapour of the three filters used. At the time of these observations, the observatory’s water vapour monitor was non-functional, and therefore there is no valid information in the data headers that could be used to deduce the observing conditions during the observations. In order to investigate this further, the raw data products were downloaded from the SOFIA data archive and processed with a custom IDL software package. These raw files contain data from each chop and nod position separately, allowing one to measure statistics related to the background emission, and by measuring these statistics in all files, one can deduce the atmospheric conditions by using the background behaviour with time as a proxy. The first flight experienced a brief episode of highly elevated background emission, which was likely due to temporary high precipitable water vapour conditions, and thus data during this episode were discarded. The second flight was almost completely plagued by highly variable backgrounds, again likely due to unusually high precipitable water vapour conditions. In addition, this second flight had some telescope pointing issues

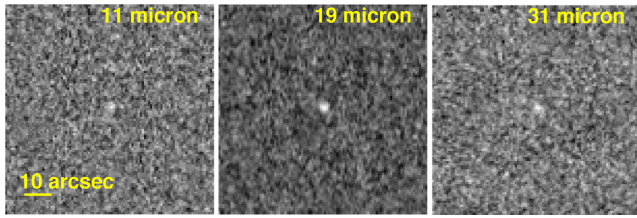
that could not be corrected in the data. The combination of these issues made it difficult to salvage any of the 11.1 and 31.5 μm data from that flight. After discarding all data flagged for problems from both flights, the remaining data were co-added, yielding final effective on-source exposure times in the three filters of 5900 s at 11.1 μm , 3900 s at 19.7 μm , and 5900 s at 31.5 μm . The final signal-to-noise measurements on the detection of SN 1987A at these three wavelengths are 6 at 11.1 μm , 11 at 19.7 μm , and 8 at 31.5 μm .

While chopping and nodding removes the vast majority of background sky and telescope emission, the large field of view of FORCAST and limited stability of in-flight observations leads to the presence of some low-frequency coherent background noise structures in the imaging data. To mitigate this, the co-added images were cropped to $78' \times 78'$, and by using a custom sky subtraction programme, a low-power (between 2 and 5), two-dimensional, polynomial surface was fitted to the background with the central source being masked out. By subtracting these background surface fits from the co-added images, the final images were created at each of the three wavelengths.

The same flux calibrations applied to the pipeline-processed data were used to calibrate the final re-processed images. The SOFIA Data Cycle System pipeline calculates the flux calibration factors (i.e. $\text{Jy ADU}^{-1} \text{ s}^{-1}$) and errors based upon standard star observations across multiple flights and observing cycles, taking into account airmass corrections for telescope elevation and aircraft altitude, and these values are given in the pipeline-processed data headers. The flux calibration errors given in the headers are: 2.8 per cent at 11.1 μm , 4.2 per cent at 19.7 μm , and 7.0 per cent at 31.5 μm . However, the dominant source of error in the flux density estimates in these particular data comes from the measurement errors due to

Table 1. *SOFIA* and *WISE* measured fluxes of SN 1987A.

Filter	λ_{eff} (μm)	$\Delta\lambda$ (μm)	Flux (mJy)
<i>SOFIA</i> day 10 732			
FOR_F111	11.1	0.95	45 ± 7
FOR_F197	19.7	5.5	88 ± 9
FOR_F315	31.5	5.7	105 ± 14
<i>WISE</i> mission between day 8330 and 8565			
W1	3.35	0.66	1.323 ± 0.038
W2	4.60	1.04	2.317 ± 0.055
W3	11.56	5.51	39.95 ± 0.68
W4	22.09	4.10	105.6 ± 3.3

**Figure 2.** *SOFIA* images of SN 1987A, showing detections of an unresolved point source in all three filter bands.

the low S/N of SN 1987A observations. The measurement errors for the aperture photometry are: 15.6 per cent at 11.1 μm , 8.8 per cent at 19.7 μm , and 11.9 per cent at 31.5 μm . Therefore, the total flux calibration errors are these two values added in quadrature for each filter. Applying these calibration factors and errors to the data produces the following measured flux densities and 1-sigma errors for SN 1987A: 45 ± 7 mJy at 11.1 μm , 88 ± 9 mJy at 19.7 μm , and 105 ± 14 mJy at 31.5 μm (Table 1).

Fig. 2 shows the *SOFIA* reduced images of SN 1987A at three bands, with detections in all bands. SN 1987A is unresolved, seen as a point source. This is expected because the full width at half-maximum (FWHM) of the point spread function at our shortest wavelength (11.7 μm) is about 2.7 arcsec (*SOFIA* Observing Handbook), which is larger than the size of the ring (~ 1.5 arcsec in diameter). The detection limit (S/N = 4) of FORCAST in the 31.5 μm band is estimated to be 105 mJy for 5900 s exposure time in dual channel mode (*SOFIA* observer's Handbook for Cycle 4). That is consistent with our detected flux – if the 31.5 μm band flux had not increased since the *Spitzer* observations, the source would be about 40 mJy, and it would not have been detected at 31.5 μm . Therefore, SN 1987A has brightened at 31.5 μm , allowing the source to be detected at this wavelength.

3 SPECTRAL ENERGY DISTRIBUTIONS

3.1 Historical spectral energy distributions

Fig. 1 shows the historical spectral energy distributions (SEDs) of SN 1987A. The last *Spitzer* measurements before its helium ran out in 2009 are plotted in red in Fig. 1. The data include the *Spitzer* IRAC four photometric bands from 3.6 to 8.0 μm at day 7974, the MIPS 24 μm flux at day 7983, and IRS spectrum from 5 to 35 μm at day 7954 (Dwek et al. 2010; Arendt et al. 2016). Dwek et al. fitted the near- and mid-infrared SED with two dust components, hot and warm (Fig. 1).

Wide-Field Infrared Survey Explorer (*WISE*) is an all-sky survey at 3.4, 4.6, 12, and 22 μm (Wright et al. 2010), with the mission life from 2009 December 14 (day 8330) and 2010 August 6 (day 8565). The magnitudes of SN 1987A were taken from the *ALLWISE* catalogue Table 1, with the filter widths taken from Jarrett et al. (2011). They were converted to fluxes without colour corrections, yielding 1.323 ± 0.038 , 2.317 ± 0.055 , 39.95 ± 0.68 , 105.6 ± 3.3 mJy at 3.4, 4.6, 12, and 22 μm , respectively. The scanned dates of SN 1987A are not listed in the catalogue, so we take the approximate date of the *WISE* scanned date as day 8450 since the explosion.

3.2 The SED at day $\sim 10\,000$

Fig. 1 shows the *SOFIA* flux measurements of SN 1987A at three bands at day $\sim 10\,732$. In order to analyse these data points, we assembled the infrared and submillimeter flux measurements from dates close to the *SOFIA* observations. The *Spitzer* warm mission measured the flux of SN 1987A, using IRAC at 3.6 and 4.5 μm , at day 10 377 (Arendt et al. 2016). The *Herschel Space Observatory* measured the flux of SN 1987A at 70, 100, 160, 250, and 350 μm at day 9090 (Matsuura et al. 2015). The ALMA fluxes of the ejecta were measured at 850 and 450 μm at day 9294 and 9351 (Zanardo et al. 2014). All these measurements are plotted in blue circles in Fig. 1.

Fig. 1 demonstrates the presence of an excess at 31.5 μm , which was not detected with *Spitzer* IRS observations 10 yr ago. An excess at 70 μm on top of the cold ejecta dust was reported by Matsuura et al. (2015). That could not be accounted for by a potential contribution of 63 μm [O I] line emission to the wide 70 μm filter. The excess found at 31.5 μm appears to continue to the 70 μm band, and we call this excess a ‘30–70 μm excess’.

Arendt et al. (2016) reported a decreasing trend for the hot dust components since day ~ 8500 , after a long term increase since day 4000. This is also found in Fig. 1 for the *Spitzer* 4.5 and *WISE* 4.6 μm fluxes. The decreasing trend is also found in the *Spitzer* 3.6 μm flux.

In contrast to the hot component, the time variation of the warm component at 8–20 μm is unclear. The *SOFIA* 11.1 μm flux at day 10 732 is consistent with the *Spitzer* IRS spectrum at day 7954 and the *WISE* 12 μm at day ~ 8450 , with the consideration that these bands are on the shoulder of silicate emission at 10 μm . The *Spitzer* MIPS 24 μm flux and the *WISE* 22 μm flux are also consistent with the *Spitzer* IRS spectra. Fig. 1 includes a 1σ uncertainty in plotting the *SOFIA* 19.7 μm flux. Although the *SOFIA* 19.7 μm flux at day 10 732 have decreased more than 1σ uncertainty since the *Spitzer* IRS spectrum were taken at day 7954, they are still consistent within 3σ uncertainties.

4 ANALYSIS

4.1 Modified blackbody fitting to the SED of day $\sim 10\,000$

In order to interpret the 30–70 μm excess, we outline the known dust components to the SED fit at day 10 000. In the optically thin case, the flux density F_ν at the frequency ν from a dust mass (M_d) is given as a modified blackbody as

$$F_\nu = M_d \frac{4\kappa_\nu \pi B_\nu}{4\pi D^2}, \quad (1)$$

where M_d is the dust mass, $B_\nu(T_d)$ is the Planck function, and T_d is the dust temperature (Hildebrand 1983). D is the distance to the

Table 2. Dust model parameters with modified black bodies.

		Hot component		Warm component		q^a	30–70 μm excess		Cold component		Figure
		M_d $\times 10^{-8} (M_\odot)$	T_d (K)	M_d $\times 10^{-5} (M_\odot)$	T_d (K)		M_d $\times 10^{-4} (M_\odot)$	T_d (K)	M_d (M_\odot)	T_d (K)	
Model 1	Day ~ 7980	2.69 ± 0.07	525.250 ± 0.008	0.900 ± 0.005	190.98 ± 0.02	–					Fig. 1
Model 2	Day $\sim 10\,000$	2.0 ± 0.3	525 ± 17	0.6 ± 0.7	191 ± 11	–	3.6 ± 2.0	85 ± 4	0.549 ± 0.08	20.3 ± 0.5	Fig. 1
Model 3	Day $\sim 10\,000$	2.0 ± 0.3	525 ± 17	3.2	150	–			0.549 ± 0.08	20.3 ± 0.5	Fig. 3
Model 4	Day $\sim 10\,000$	2.0 ± 0.2	525 ± 13	0.6 ± 0.3	191 ± 5	–	3.9 ± 8.0	85 ± 17	0.493 ± 0.10	20.4 ± 0.3	Fig. 4
Model 5	Day ~ 7980	2.69 ± 0.07	525.250 ± 0.008	$1.6^b \pm 0.1$	$195^b \pm 1$	$3.9^b \pm 0.3$					Fig. 5
Model 6	Day $\sim 10\,000$	2.0 ± 0.3	525 ± 17	$74^b \pm 40$	$187^b \pm 15$	$2.4^b \pm 1.8$			0.549 ± 0.08	20.3 ± 0.3	Fig. 5

^aUnless specified, q is fixed to 3.5. The models 2 and 4 have an additional component to explain the 30–70 μm excess: the model 2 uses only three components (hot, warm, and 30–70 μm excess) to fit 3.6–70 μm fluxes, with fixed parameters of the cold component, while the model 4 consider all four components as independent parameters, fitting 3.6–870 μm fluxes. The model 3 is to find a solution of the hot component in order to fit 11.1–31.5 μm SOFIA data within 3- σ , instead of 1- σ uncertainty. The model 5 and 6 use temperature dependence of grain size for warm dust, and the temperature quoted here is for the highest temperature (for the smallest grains). ^bTemperature gradient of collisionally heated grains was considered.

LMC, adopted to be 50 kpc. The dust mass absorption coefficient $\kappa_{\nu,a}$ is expressed as $\kappa_{\nu,a} = 3Q_v/4\rho a$, where ρ is the mass density of the dust grains, Q_v is the dust emissivity at the frequency ν , and a is the grain size. In the Rayleigh limit, i.e. the grain size a is much smaller than the emitting wavelength (λ), $a \ll \lambda$, κ_v can be simply expressed by a power-law $\kappa \propto \lambda^{-\beta}$, for spherical grains, without grain size dependence. Thus, the flux F_ν becomes independent of the grain size, at a given dust temperature T_d .

For hot and warm components, Dwek et al. (2010) and Arendt et al. (2016) already made fits to the *Spitzer* day ~ 7980 fluxes. Using, the IDL χ^2 minimization procedure, AMOEBA (Press et al. 2002), we searched for parameters that can fit these photometric bands and spectra with two components. Uncertainties were estimated by Monte Carlo method (Press et al. 2002). These two-components (hot and warm) were simultaneously fitted. The fitted results and uncertainties were cross-checked with those with an independent IDL fitting code, MPFIT (Markwardt 2009). The adopted parameters of the hot and warm components are summarized in models 1 and 2 of Table 2, and plotted in Fig. 1. Dwek et al. tested four different types of dust compositions for the hot component, and in our analysis, amorphous carbon (Roubeau & Martin 1991) is used. The difference in the fitted temperature of the hot component at day ~ 7000 is mainly due to assumed grain size: Dwek et al. estimated the grain size distribution from X-ray flux, while we fixed the grain size at 0.1 μm , focusing on infrared flux only. The IRS spectra clearly showed silicate features, and fitting of the warm component used the optical constants from Draine & Lee (1984) and Laor & Draine (1993). The derived parameters of the warm component is marginally different from those by Dwek et al., showing little impact of the parameter difference of the hot component on those of the warm component.

Cold ejecta dust was reported by Matsuura et al. (2015), and their *Herschel* flux measurements were about four and half years before the SOFIA measurements. Matsuura et al. (2011) suggested that the heating source of the ejecta dust is most likely due to ^{44}Ti decay. The half-life of ^{44}Ti is estimated to be 85 yr (Jerkstrand, Fransson & Kozma 2011), and the heating from ^{44}Ti decay would have declined only by 4 per cent over this four and half year time. Therefore, it is most likely that the luminosity of the ejecta dust has changed little since the *Herschel* measurements within their uncertainties. In Fig. 1, the fitting with amorphous carbon (Zubko et al. 1996) is plotted. This is a fitting to *Herschel* 100–350 μm and ALMA 450 & 850 μm fluxes (Zanardo et al. 2014), and an independent fitting from the hot and warm components. Matsuura et al. (2015) tested fitting the cold ejecta dust with amorphous silicates (Jäger et al. 2003), but the difference in the predicted 70 μm fluxes between these two dust

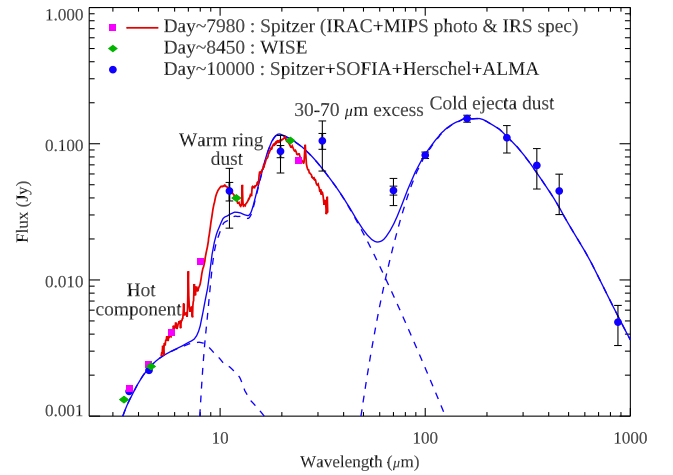


Figure 3. Fitting the SEDs within the 3- σ uncertainties of the SOFIA fluxes (Table 2, model 3). Both 1- σ and 3- σ uncertainties are plotted for the SOFIA fluxes and *Herschel* 70 μm , while the uncertainties for the *Herschel* and ALMA bands at >100 μm remain 1- σ only, the same as Fig. 1. The *Spitzer*'s uncertainties are smaller than the plotting symbols. By increasing the dust mass and decreasing the dust temperature of the warm component, the SOFIA 11–31 μm fluxes can be fitted within the 3- σ uncertainties, but this fit is insufficient to reproduce the 70 μm excess.

models is negligible (only a 4 per cent difference). Thus, adopting different dust compositions does not affect our conclusion of having an excess at 70 μm .

After fitting the warm ring dust and cold ejecta dust, the excess departs from 30 to 70 μm at a $>6\sigma$ level.

In order to verify the presence of the excess, we further made a single component fit to the SOFIA 11.1, 19.7, and 31.5 μm fluxes, considering their 3- σ level uncertainties. As is found in Fig. 3, a warm component with a dust temperature of 150 K and a dust mass of $3.2 \times 10^{-5} M_\odot$ (model 3 in Table 2) can fit the SOFIA 11.1, 19.7, and 31.5 μm fluxes within 3- σ uncertainties. In this fit, we vary only the parameters of the warm component, with those of hot and cold components fixed as of model 2. However, this model spectrum underpredicts the *Herschel* 70 μm excess by a factor of 6; even with cold ejecta dust, this model still underpredicts the flux by a factor of 2. We further attempted to search for a fit to the SOFIA bands and the *Herschel* 70 μm excess with the χ -square minimization procedure AMOEBA, but no solution was found within the 3- σ uncertainties. A warm component with a modified blackbody fit is insufficient to reproduce the 11–70 μm fluxes.

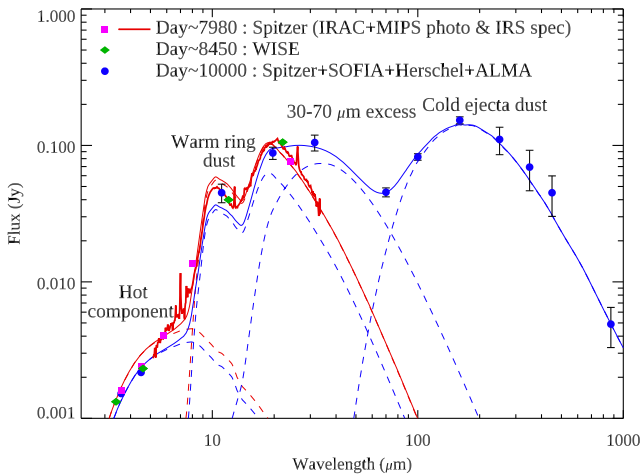


Figure 4. SEDs and fitted results to day $\sim 10\,000$ with all four components as independent parameters (Table 2 model 4).

4.2 An additional ‘30–70 μm ’ component?

In order to understand the nature of the 30–70 μm excess, we further model it with an additional modified blackbody component, while we kept the parameters of hot, warm, and cold as explained in the previous section. The 30–70 μm excess requires the dust temperature to be 85 K and the dust mass to be $3.6 \times 10^{-4} M_{\odot}$ (Table 2, model 2; Fig. 1) assuming silicate dust (Draine & Lee 1984). In this model, we fitted the ‘excess’ on top of the warm and cold components. The temperature of 85 K is between those of the warm and cold components. The dust mass from the best-fitted parameters is about a factor of 300 larger than that of the warm component. Because the *Planck* Function is involved in equation (1) and because lower dust temperature yields lower luminosity, the ~ 85 K excess would require a much higher dust mass than the ~ 191 K warm component, even though the uncertainty in the dust mass of the excess component is large.

Finally, we fit all four components simultaneously as free parameters, and the fitted results are summarized in Table 2 model 4 and shown in Fig. 4. The best-fitted parameters are consistent with the fitting of three components (hot, warm, and cold) and an additional ‘30–70 μm ’ excess on top (Table 2 model 2), however, the fitting does not converge well, resulting in large uncertainties in the dust mass on the excess component.

4.3 Alternative possibility – temperature gradient and large grains in warm component?

4.3.1 Temperature gradient

While equation (1) assumes that all dust grains have the same dust temperature, this assumption might not be always the best, and may potentially be an oversimplification. We consider an alternative possibility that dust grains in the warm component have a temperature gradient as a function of grain size, resulting in a wider spread in the emitting wavelengths.

The ring dust can be continuously heated by X-ray radiation, emitted by the interaction between the fast SN blast wave with the pre-existing equatorial ring (Bouchet et al. 2006; Dwek et al. 2010; Frank et al. 2016). The fastest part of the ejecta gas expanded with a speed of over 3000 km s^{-1} (McCray 1993; Larsson et al. 2016), and has caught up with the slower (100 km s^{-1} ; Groningsson

et al. 2008) expanding ring. In the shocked ring, there are two possible grain heating mechanisms, collisional heating by shocked gas and radiative heating in the radiative shocks (Bouchet et al. 2006). Dwek et al. (2008) mainly considered collisional heating and noted that the heating rate depends on whether electrons from the X-ray plasma stopped inside the grains or ‘penetrate’, and that the grain temperature depends on grain size only when the electrons are trapped inside the grains. Approximately, the temperature of a dust grain of a radius a is a function of $a^{-\gamma}$, where $\gamma = 1/(4 + \beta)$. Although this approximation is not accurate for the near-infrared, the overall shape of the SED at mid-infrared and far-infrared wavelengths does not have a significant impact due to this approximation.

First, we attempted to fit the SED from 10–70 μm at day $\sim 10\,000$, by including the grain size dependence of the dust temperature in the warm component. The minimum and maximum grain sizes of 0.0003 and $1.0 \mu\text{m}$ were adopted (Weingartner & Draine 2001). Such a model can fit the SED from 10 to 30 μm within the $3\text{-}\sigma$ flux uncertainties. However, the model spectrum underpredicts the flux at 70 μm , almost identically to the model spectra shown in Fig. 3.

4.3.2 Temperature gradient with non-standard grain size distribution

Although we added a simple function for the temperature dependence on grain size, using only the power-law index of q of 3.5 for the Galactic ISM (Mathis, Rumpl & Nordsieck 1977), the fitted result underpredicted the flux at 70 μm . As the next step, we parametrize the power-law index q of the grain size distribution, because increasing the number of larger dust grains can further increase the fluxes at longer wavelength. We started by fitting the warm component at day ~ 8000 with a power-law index q of 3.5. The minimum and maximum grain sizes of 0.0003 and $1.0 \mu\text{m}$ were adopted (Weingartner & Draine 2001). The maximum dust temperature (i.e. the dust temperature of the smallest grain) of 195 K for the warm component can fit the SED at day ~ 8000 (model 5 in Table 2). During this process, the hot component still kept as model 1, as having only two photometry points is insufficient to introduce additional parameter of q . The resultant spectra are shown as red lines in Fig. 5.

Using the χ^2 fitting function AMOEBA, we found that the spectra using a power-law index $q = 2.4$ with a maximum dust temperature of 187 K can fit the 30–70 μm excess for day $\sim 10\,000$ (Fig. 5). The fit is slightly larger than $1\text{-}\sigma$ uncertainty at 30 μm but within $3\text{-}\sigma$. We fixed the minimum and maximum grain sizes to be 0.003 and $1 \mu\text{m}$, as we have only four photometric points, allowing optimizations of only up to three parameters (dust mass, temperature, and the power-law index of the grain-size distribution). The inferred dust mass was $7.4 \times 10^{-4} M_{\odot}$ (Table 2 model 6). Although there is a large uncertainty in the dust mass and the inferred dust mass decreases with presence of more large dust grains (smaller q index), it is another issue whether such large dust grains, i.e. nearly flat grain size distribution across grain sizes, are plausible or not.

5 DISCUSSION – ORIGIN OF THE 30–70 MICRON EXCESS

We have found emission at 30–70 μm in excess on top of previously modelled composed of hot, warm, and cold components. We note that we consider it very unlikely that strong line emission could be a contributor to the rising 30 μm flux. *Spitzer* IRS spectra did show a

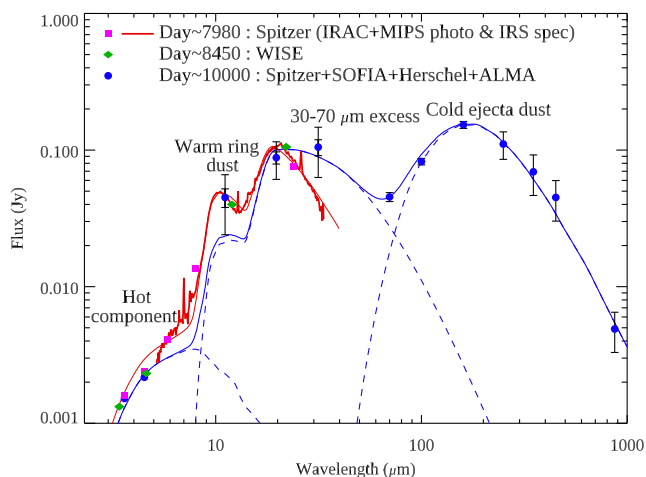


Figure 5. Fitting the SEDs with models involving grain size distributions (q) and the grain size dependent temperature for the warm component, with parameters summarized in Table 2 models 5 and 6. The models for the hot and cold components remains the modified blackbody.

weak [S III] line at 33.5 μm , which falls within the SOFIA 31.5 μm band. Additionally, [S III] has a line at 18.7 μm . If the increase of the SOFIA 31.5 μm flux is due to [S III] line, then the SOFIA 19.7 μm band flux should have increased as well. However, such an increased trend was not found at 19.7 μm . It is unlikely that the line emission is the source of the increasing 30 μm flux.

We find two possibilities for the excess emission at 30–70 μm ; model 2 an extra component at 30–70 μm on top of the previously known hot, warm, and cold components, or model 6 having a warm component with more large dust grains than the standard ISM grain size distributions. In both cases, the best-fitted parameters of the 30–70 μm emitting source have a dust mass higher than that of the warm component at day ~ 8000 . We discuss the possible interpretations of these components and associated locations.

If the excess is explained with an extra component, the excess can be fitted with a modified blackbody of an approximate temperature of 85 K (models 2 and 4). The inferred dust mass is $3.6 \times 10^{-4} M_{\odot}$ and more than 10 times larger than the mass of the warm ring dust. Because lower temperature of the modified blackbody results in lower brightness (equation 1), much higher dust mass in the excess component (temperature of ~ 85 K) would be required than that of the warm component (191 K warm). We argue that this excess might have originated from re-formed dust grains or from grain growth in the ring in the post-shock region. Dust reformation refers to dust grains formed from the gas phase, whereas dust growth refers to dust grains with increased mass due to accretion of atoms from the gas phase. Dust growth can accompany coagulation of grains with other dust grains, increasing grain sizes.

The fastest part of the blast wave started its interaction with the ring in 1995 (Sonneborn et al. 1998), and since then the morphology of the ring has changed in time; initially the shape of the ring was smooth, but eventually it broke up into clumps, and now the blast wave (forward shock) has passed the ring (Fransson et al. 2015). The pressure behind the forward shock created reverse shock propagating into the SN ejecta (Chevalier & Fransson 2016). The reverse shock caused by this interaction has been detected since 2003 (France et al. 2010). As the forward shock expands outwards, the reverse shock moves inwards, the material left in between the two shocks can cool down, and this material might be the site of dust re-formation.

A similar process but at a much earlier time frame has been proposed for type II n SNe (e.g. Smith, Foley & Filippenko 2008). Type II n SNe show narrow line emission after the explosion, and these lines indicate the presence of dense circumstellar material that had been expelled by the progenitor star before the explosion. The optical line asymmetries and the infrared excess have suggested formation of dust in the dense shell of type II n SNe, approximately a few ten to a few hundred days after the explosion (Smith et al. 2008; Fox et al. 2009; Gall et al. 2014; Andrews et al. 2016; Chugai 2018). Similar dust formation in the material between the reverse and forward shocks might happen in SN 1987A, but on a much longer time-scale than for type II n SNe.

Following the detection of CO molecules in the reverse shocked region in the Galactic SNR, Cassiopeia A (Rho et al. 2009, 2012), chemical models have been developed to explain the presence of the CO molecules from ejecta material in the post-shocked region (Biscaro & Cherchneff 2014). However, the same chemical model predicts that dust is not easily formed in the post-shock regions. Biscaro & Cherchneff (2014) modelled a type II b SN, and found that the density in the post-shock regions is not sufficiently high enough for dust formation. Furthermore, another chemical modelling (Sarangi, Dwek & Arendt 2018) of interaction between the circumstellar and SN blast winds (forward shock) in type II n SNe found that the temperature in the post-shocked region is too high for early dust formation, when dust emission has been reported as early as day 87 in SN 2010jl. If the density and the temperature are the key, that would open up a question of the density and temperature in post-shocked region in the circumstellar envelope in SN 1987A. Estimate of the time evolution of the temperature and the density of SN 1987A ring and chemical model on these physical conditions would be helpful if it is feasible for the dust formation in the SN 1987A ring.

An alternative possibility to explain the 30–70 μm excess is due to large dust grains (model 6). Compared with the power-law index of $a^{-3.5}$ for the standard ISM dust grain distributions, where a is the grain size, the excess of SN 1987A might be explained with $a^{-2.4}$, i.e. much more heavily weighted to larger dust grains than the standard ISM grain distribution.

SNR models have predicted that the power-law index q might depart from 3.5 in shocked SNRs (Bianchi & Schneider 2007; Nozawa et al. 2007; Hirashita & Kuo 2011). The model of Nozawa et al. (2007) showed that smaller dust grains are likely to be destroyed by shocks, while larger dust grains can survive. It is possible that the grain size distribution in the shocked circumstellar ring in SN 1987A might not follow a standard ISM power-law index of 3.5.

However, the inferred dust mass ($7.4 \times 10^{-4} M_{\odot}$) at day ~ 10000 is much larger than the mass ($1 \times 10^{-5} M_{\odot}$) at day ~ 8000 . That cannot be explained only by dust destruction processes, and requires dust reformation or grain growth.

The inferred dust mass to explain the 30–70 μm region has a larger dust mass than the warm component at day ~ 8000 . The timing coincides with passage of the forward shock beyond the ring, so it might be associated with forward shock.

It is unclear whether the excess found by SOFIA is dust reformation or dust growth, as we are unable to disentangle these two cases from existing data. After the passage of forward shocks into the ring of SN 1987A, existing red-supergiant dust in the circumstellar ring should have been destroyed. That would release refractory elements into gas. Dust grains can be condensed from gas, i.e. re-forming dust grains in the post-shock region. The passage of the forward shock will destroy dust grains in the circumstellar ring, but dust grains are not completely destroyed, particularly larger grains.

Surviving dust grains could offer seeds for atoms to stick on to, allowing the dust grain mass to increase with time.

The time-scale for the dust reformation might be an issue. The cooling time-scale in the shocked gas in the ring of SN 1987A has been predicted to be 12–40 yr (Dwek et al. 2010). Since the forward shocks have been interacting until recently (France et al. 2010), the cooling time-scale needs to be much shorter than that.

An alternate possibility is that the 30–70 μm excess is associated with the SN ejecta. The decreasing density of heavy elements will allow X-rays to heat an increasingly larger mass of ejecta dust to higher temperatures. These possibilities will be tested by the forthcoming *JWST* space mission. MIRI on board the *JWST* has a wavelength coverage up to 28 μm , and it has an angular resolution sufficient to resolve the inner structure of the ring and ejecta. Thus, MIRI should be able to pin down exactly the location of the 30–70 μm excess, whether it is within the ejecta, or whether it is in dense material between the forward and reverse shock within the ring clumps.

If the dust mass can increase in post-shock regions, the roles of SNe on dust evolution of galaxies might be re-evaluated. Our observations suggest that it might be much easier to form dust grains than previously thought in a SN environment. SNe have been discussed concerning their roles on largely destroying ISM dust with forward shocks, and as a source of ISM dust because newly formed dust can be formed from newly synthesised elements in the ejecta, although such dust has been suggested to be completely destroyed by reverse shocks (Bianchi & Schneider 2007; Nozawa et al. 2007). Having dust forming in post-shock regions could potentially cause a re-evaluation of the overall dust input from SNe and SN remnants into the interstellar medium.

6 CONCLUSIONS

We report SOFIA flux measurements of SN 1987A at 11.1, 19.7, and 31.5 μm in 2016. We found that the 31.5 μm flux has increased since *Spitzer* measurements 10 yr earlier. Together with the excess found by *Herschel* at 70 μm , we consider the origin of 30–70 μm continuum excess. That excess can be fitted with dust component with a temperature of about 85 K dust and with a dust mass of $3.5 \times 10^{-4} M_{\odot}$. We suggest that the 30–70 μm excess might be due to the dust re-formation in the circumstellar ring, after the passage of the forward shocks. An alternative possibility is that part of the ejecta dust could be being heated to a much higher temperature than the rest of the ejecta dust. If the 30–70 μm excess is indeed due to dust re-formation, that would suggest that dust formation or grain growth might take place much more easily and widely than previously thought.

ACKNOWLEDGEMENTS

Based on observations made with the NASA/DLR Stratospheric Observatory for Infrared Astronomy (SOFIA). SOFIA is jointly operated by the Universities Space Research Association, Inc. (USRA), under NASA contract NAS2-97001, and the Deutsches SOFIA Institut (DSI) under DLR contract 50 OK 0901 to the University of Stuttgart. Financial support for this work was provided by NASA through SOFIA 04-0016 issued by USRA. This publication makes use of data products from the Wide-field Infrared Survey Explorer, which is a joint project of the University of California, Los Angeles, and the Jet Propulsion Laboratory/California Institute of Technology, funded by the National Aeronautics and Space Administration. This work is based (in part) on archival data obtained with the

Spitzer Space Telescope, which is operated by the Jet Propulsion Laboratory, California Institute of Technology under a contract with NASA. Support for this work was provided by an award issued by JPL/Caltech. MM acknowledges support from STFC Ernest Rutherford fellowship (ST/L003597/1), MJB, AB, and RW acknowledge support from European Research Council (ERC) Advanced Grant SNDUST 694520, and HLG and PC acknowledge support from the European Research Council (ERC) in the form of Consolidator Grant COSMICDUST (ERC-2014-CoG-647939).

REFERENCES

- Andrews J. E. E. et al., 2016, *MNRAS*, 457, 3241
 Arendt R. G. et al., 2010, *ApJ*, 725, 585
 Arendt R. G., Dwek E., Bouchet P., Danziger I. J., Frank K. A., Gehrz R. D., Park S., Woodward C. E., 2016, *AJ*, 151, 62
 Arnett W. D., Bahcall J. N., Kirshner R. P., Woosley S. E., 1989, *ARA&A*, 27, 629
 Barlow M. J., 1978, *MNRAS*, 183, 367
 Bevan A., Barlow M. J., 2016, *MNRAS*, 456, 1269
 Bianchi S., Schneider R., 2007, *MNRAS*, 378, 973
 Biscaro C., Cherchneff I., 2014, *A&A*, 564, A25
 Bocchio M., Jones A. P., Slavin J. D., 2014, *A&A*, 570, A32
 Bouchet P., De Buizer J. M., Suntzeff N. B., Danziger I. J., Hayward T. L., Telesco C. M., Packham C., 2004, *ApJ*, 611, 394
 Bouchet P. et al., 2006, *ApJ*, 650, 212
 Chevalier R. A., Fransson C., 2016, in Alsabti A. W., Murdin O., eds, *Handbook of Supernovae*, Springer International Publishing, Switzerland, 875
 Chugai N. N., 2018, *MNRAS*, 481, 3643
 Danziger I., Gouffes C., Bouchet P., Lucy L. B., 1989, *IAU Circular No. 4747*, Supernova 1987a in the Large Magellanic Cloud. Kluwer, Dordrecht
 Draine B. T., Lee H. M., 1984, *ApJ*, 285, 89
 Dwek E., Arendt R. G., 2015, *ApJ*, 810, 75
 Dwek E., Cherchneff I., 2011, *ApJ*, 727, 63
 Dwek E. et al., 2008, *ApJ*, 676, 1029
 Dwek E. et al., 2010, *ApJ*, 722, 425
 Fox O. et al., 2009, *ApJ*, 691, 650
 France K. et al., 2010, *Science*, 329, 1624
 Frank K. A., Zhekov S. A., Park S., McCray R. A., Dwek E., Burrows D. N., 2016, *ApJ*, 829, 40
 Fransson C. et al., 2015, *ApJ*, 806, L19
 Gall C. et al., 2014, *Nature*, 511, 326
 Groningsson P., Fransson C., Leibundgut B., Lundqvist P., Challis P., Chevalier R. A., Spyromilio J., 2008, *A&A*, 492, 481
 Herter T. L. et al., 2012, *ApJ*, 749, L18
 Hildebrand R. H., 1983, *Q. J. R. Astron. Soc.*, 24, 267
 Hirashita H., Kuo T.-M., 2011, *MNRAS*, 416, 1340
 Indebetouw R. et al., 2014, *ApJ*, 782, L2
 Jäger C., Dorschner J., Mutschke H., Posch T., Henning T., 2003, *A&A*, 408, 193
 Jarrett T. H. et al., 2011, *AJ*, 735, 112
 Jerkstrand A., Fransson C., Kozma C., 2011, *A&A*, 530, A45
 Jones A. P., Tielens A. G. G. M., Hollenbach D. J., McKee C. F., 1994, *ApJ*, 433, 797
 Kotak R. et al., 2009, *ApJ*, 704, 306
 Lakićević M. et al., 2015, *ApJ*, 799, 50
 Laor A., Draine B. T., 1993, *ApJ*, 402, 441
 Larsson J. et al., 2016, *ApJ*, 833, 147
 Lau R. M., Herter T. L., Morris M. R., Li Z., Adams J. D., 2015, *Science*, 348, 413
 Markwardt C. B., 2009, in Bohlender D. A., Durand D., Dowler P., eds, *ASP Conf. Ser. Vol. 411, Astronomical Data Analysis Software and Systems XVIII, Non-linear Least-squares Fitting in IDL with MPFIT*. Am. Inst. Phys., New York, p. 251
 Mathis J. S., Rumpel W., Nordsieck K. H., 1977, *ApJ*, 217, 425

- Matsuura M., 2017, in Alsabti W., Murdin P., eds, *Handbook of Supernovae*. Springer International Publishing, Switzerland, p. 2125
- Matsuura M. et al., 2011, *Science*, 333, 1258
- Matsuura M. et al., 2015, *ApJ*, 800, 50
- Matsuura M. et al., 2016, *MNRAS*, 462, 2995
- McCray R. A., 1993, *ARA&A*, 31, 175
- Micelotta E. R., Matsuura M., Sarangi A., 2018, in Bykov A. M., Chevalier R. A., Falanga M., Raymond J. C., von Steiger R., eds, *Supernovae*. Springer, Netherlands, p. P53
- Morgan H. L., Edmunds M. G., 2003, *MNRAS*, 343, 427
- Nozawa T., Kozasa T., Umeda H., Maeda K., Nomoto K., 2003, *ApJ*, 598, 785
- Nozawa T., Kozasa T., Habe A., Dwek E., Umeda H., Tominaga N., Maeda K., Nomoto K., 2007, *ApJ*, 666, 955
- Press W. H., Teukolsky S. A., Vetterling W. T., Flannery B. P., 2002, *Numerical Recipes in C++: The Art of Scientific Computing*. Cambridge Univ. Press, Cambridge
- Rho J., Jarrett T. H., Reach W. T., Gomez H. L., Andersen M., 2009, *ApJ*, 693, L39
- Rho J., Onaka T., Cami J., Reach W. T., 2012, *ApJ*, 747, L6
- Rouleau F., Martin P. G., 1991, *ApJ*, 377, 526
- Sankrit R. et al., 2010, *ApJ*, 712, 1092
- Sarangi A., Dwek E., Arendt R. G., 2018, *ApJ*, 859, 66
- Sarangi A., Matsuura M., Micelotta E. R., 2018, *Space Sci. Rev.*, 214, 63
- Schneider R., Ferrara A., Salvaterra R., 2004, *MNRAS*, 351, 1379
- Silvia D. W., Smith B. D., Shull J. M., 2012, *ApJ*, 748, 12
- Slavin J. D., Dwek E., Jones A. P., 2015, *ApJ*, 803, 7
- Sluder A., Milosavljević M., Montgomery M. H., 2018, *MNRAS*, 480, 5580
- Smith N., Foley R. J., Filippenko A. V., 2008, *ApJ*, 680, 568
- Sonneborn G. et al., 1998, *ApJ*, 492, L139
- Temim T., Dwek E., Tchernyshyov K., Boyer M. L., Meixner M., Gall C., Roman-Duval J., 2015, *ApJ*, 799, 158
- Wallström S. H. J. et al., 2013, *A&A*, 558, L2
- Weingartner J. C., Draine B. T., 2001, *ApJ*, 548, 296
- Werner M. W. et al., 2004, *ApJS*, 154, 1
- Wesson R., Barlow M. J., Matsuura M., Ercolano B., 2015, *MNRAS*, 446, 2089
- Wooden D. H., Rank D. M., Bregman J. D., Witteborn F. C., Tielens A. G. G. M., Cohen M., Pinto P. A., Axelrod T. S., 1993, *ApJS*, 88, 477
- Wright E. L. et al., 2010, *AJ*, 140, 1868
- Young E. T. et al., 2012, *Proc. SPIE Conf. Ser. Vol. 8444, Ground-based and Airborne Telescopes IV, Early Science Results from SOFIA*. SPIE, Bellingham, p. 844410
- Zanardo G. et al., 2014, *ApJ*, 796, 82
- Zubko V. G., Mennella V., Colangeli L., Bussoletti E., 1996, *MNRAS*, 282, 1321

This paper has been typeset from a \LaTeX file prepared by the author.